HHS Public Access

Author manuscript

Cancer Res. Author manuscript; available in PMC 2023 September 02.

Published in final edited form as:

Cancer Res. 2023 March 02; 83(5): 686–699. doi:10.1158/0008-5472.CAN-22-2042.

HAND2 assists MYCN enhancer invasion to regulate a noradrenergic neuroblastoma phenotype

Man Xu[1], **Ming Sun**[1], **Xiyuan Zhang**[1], **Rosa Nguyen**[1], **Haiyan Lei**[1], **Jack F. Shern**[1], **Carol J. Thiele**[1,*], **Zhihui Liu**[1,*]

[1]Pediatric Oncology Branch, National Cancer Institute, Bethesda, MD, USA

Abstract

Noradrenergic neuroblastoma (NB) is characterized by a core transcriptional regulatory circuitry (CRC) comprised of transcription factors (TFs) such as PHOX2B, HAND2 and GATA3, which form a network with MYCN. At normal physiologic levels, MYCN mainly binds to promoters but when aberrantly upregulated as in NB, MYCN also binds to enhancers. Here, we investigated how MYCN invades enhancers and whether CRC TFs play a role in this process. HAND2 was found to regulate chromatin accessibility and assist MYCN binding to enhancers. Moreover, HAND2 cooperated with MYCN to compete with nucleosomes to regulate global gene transcription. The cooperative interaction between MYCN and HAND2 could be targeted with an Aurora A kinase inhibitor plus a histone deacetylase inhibitor, resulting in potent downregulation of both MYCN and the CRC TFs and suppression of *MYCN*-amplified NB tumor growth. This study identifies cooperation between MYCN and HAND2 in NB and demonstrates that simultaneously targeting MYCN and CRC TFs is an effective way to treat this aggressive pediatric tumor.

INTRODUCTION

Distinct combinations of TFs need to work together to specifically bind to DNA and precisely regulate gene transcription (1). Transcriptional dysregulation is a hallmark of many cancers where *MYC* family gene amplification and translocation disrupt transcriptional programs in normal development (2). Under physiological conditions, MYC or MYCN transcription factor (TF) mainly binds to promoter regions. However, in cancer cells, aberrantly elevated MYC or MYCN binds to both gene promoters with canonical E-box motifs and enhancers containing low-affinity non-canonical E-boxes (3–5). This enhancer invasion is hypothesized to be one of the mechanisms by which aberrantly elevated MYC or MYCN drives tumorigenesis.

MYCN amplification occurs in tumors from patients with neuroblastoma (NB), a tumor arising from neural crest sympathoadrenal derivatives and marks high-risk disease (6,7).

*To whom correspondence should be addressed. Zhihui Liu: National Cancer Institute; Building 10, CRC, Room 1W-5816; 10 Center Dr. MSC-1105; Bethesda, MD 20892; Tel: 1-240-858-3857; Fax: 1-301-451-7052; liuzhihu@mail.nih.gov., Carol J. Thiele: National Cancer Institute; Building 10, CRC, Room 1W-5816; 10 Center Dr. MSC-1105; Bethesda, MD 20892; Tel: 1-240-858-3849; Fax: 301-451-7052; thielec@mail.nih.gov.

Conflict of interest

The authors declare no conflict of interest

Studies indicate NB subverts a subset of neural crest lineage specific TFs including PHOX2B, HAND2, GATA3 and ASCL1 to form a core transcriptional regulatory circuitry (CRC) in noradrenergic NB (8–12). MYCN invades enhancers and decreases in *MYCN* expression depleted genome bound TWIST1 at enhancers (5). However, mechanisms by which MYCN invades enhancers are ill-defined. Since the studies on gene transcription models indicate that small numbers of TFs work together to achieve specific DNA binding (1,13), we hypothesize that the CRC TFs assist MYCN to bind enhancers to govern a noradrenergic NB tumor phenotype.

Here, we demonstrate that the CRC TF HAND2 facilitates MYCN enhancer invasion. HAND2 regulates chromatin accessibility and cooperates with MYCN to control global gene expression. More importantly our findings indicate the need to target CRC TFs simultaneously in combination with MYCN to increase the efficacy of cancer therapies. Indeed, the use of an Aurora A kinase inhibitor plus a HDAC inhibitor to target both MYCN and the CRC TFs synergistically suppresses NB growth in *MYCN*-amplified cell lines.

MATERIALS AND METHODS

Cell culture

Human embryonic kidney cells (HEK293T) and Lenti-X HEK293 were obtained from ATCC and were maintained in Dulbecco's modified Eagle's media. Human neuroblastoma cell lines IMR32, IMR5, KCNR, LAN5, LAN6 and SK-N-FI were obtained from the cell line bank of the Pediatric Oncology Branch of the National Cancer Institute and have been genetically verified. All the NB cell lines were maintained in RPMI-1640 medium. All the cell culture medium was supplemented with 10% fetal calf serum (FBS), 100 μg/mL streptomycin, 100 U/mL penicillin, and 2 mM L-glutamine. Cells were grown at 37°C with 5% CO2. All cell lines were frequently assayed for *Mycoplasma* using MycoAlert Kit (Lonza) to ensure they were free of *Mycoplasma* contamination. The cell lines used were within 12 passages after thawing.

Plasmids and stable clones

To generate Hs_3_siHAND2 resistant HAND2 constructs, HAND2 coding sequence with mutated nucleotides that cannot be recognized by Hs_3_siHAND2 and without changes in the amino acid code was synthesized by IDT company (Table S1). The HAND2 mutant (HAND2mut) open reading frame was cloned into the doxycycline inducible pLVX-pTetOne-puro vector (Takara Bio) using In-Fusion HD (Takara Bio) following the manufacturer's manual. By using the same approach, MYCN open reading frame (Table S1) was cloned into pLVX-pTetOne-puro vector. IMR32 cells were infected with lentiviral particles generated using either empty pLVX-TetOne-Puro vector or the pLVX-TetOne-Puro-HAND2mut vector, or pLVX-TetOne-Puro-MYCN vector followed by puromycin selection. The stable clones named as IMR32tetEV, IMR32tetHAND2mut and IMR32tetMYCN respectively. HAND2 and MYCN expression in IMR32tetHAND2mut could be induced with 0.025–0.1 μg/ml Dox treatment.

Realtime PCR

The RNeasy Plus Mini Kit (Qiagen) was used to collect the mRNA according to the manufacturer's protocol. Quantitative measurements of total β-actin and other genes' levels were obtained using the BIO-RAD CFX Touch realtime PCR detection system and performed in triplicate. Ct values were standardized to β-actin levels. Representative data from biological replicates were shown in this study. Primer sequences used for realtime PCR are shown in Table S1.

CRISPR-Cas9 mediated gene knockout

IMR32 cells were transduced with the lentivirus of Edit-R Dox Inducible Lentiviral Cas9 (Dharmacon, Waltham, MA) followed by blasticidin selection (5 μg/ml). Guide RNA (gRNA) that target the exon of human *HAND2* gene (sgHAND2) (Table S2) was designed, synthesized and cloned into the pLentiGuide-Puro vector (GenScript, Piscataway NJ). The Dox-inducible Cas9-expressing IMR32 cells were transduced with sgHAND2 or non-targeting control gRNA (sgCtrl) lentiviral particles (MOI=10) and selected with puromycin (0.5 μg/ml). IMR32Cas9-sgCtrl or IMR32Cas9-sgHAND2 cell line was further single clone selected from the pool and cells are maintained in complete RPMI-1640 containing 0.5ug/ml puromycin.

Transient transfection

Transient transfection was performed as described previously (14). siRNAs were purchased from Qiagen or GE Dharmacon company (Table S2). siRNAs were transiently transfected into NB cells using Nucleofector electroporation (Lonza): solution L and program C-005 for IMR32 and IMR5; solution V and program A-030 for the rest NB cell lines.

Cell growth and neurite extension assay

To evaluate cell proliferation, NB cells were plated in 96-well plates and the growth kinetics were monitored in IncuCyte ZOOM (Essen BioScience) using the integrated confluence algorithm as a surrogate for cell number. An alternative approach is to use CellTiter-Glo (Promega) to perform cell viability assay. Cell neurite length was measured using Essen IncuCyte ZOOM neurite analysis software. SynergyFinder online tool (RRID:SCR_019318) was used to study the synergistic effect of the combination treatment of NB cells *in vitro*.

Soft agar clonogenic assay

To assess the effects of the loss of *HAND2* on anchorage independent cell growth, 1×10^4 IMR32Cas9-sgCtrl or IMR32Cas9-sgHAND2 cells were cultured in 0.7% top agarose in media on a layer of 1.4% bottom agar/media to prevent the adhesion of cells to the culture plates. Medium was changed twice a week with or without 0.5 μg/mL Dox, and the number of visible colonies was counted after crystal violet staining after 3 weeks culture.

Protein isolation and western blotting analysis

For assessment of protein levels, cells were lysed using RIPA buffer, and 10 μg of total protein was separated and electroblotted as described previously (15). Protein bands probed with diluted primary antibodies (Table S3) were detected using a goat anti-rabbit or mouse

IgG-HRP conjugated secondary antibody (200 μg/mL; Santa Cruz Biotechnology) and visualized using enhanced chemiluminescence (Amersham Biosciences).

RNA-seq

Total RNA was isolated from IMR32 and LAN5 cells that have been transiently transfected with different siRNAs or siCtrl for 72 h and subjected to RNA-seq analysis as previously described (16). Each sample had 3 biological repeats. Statistical results of differentially expressed genes from Partek Flow, or Parteck Genomics Suite v7.17 or DESeq2 (RRID:SCR_000154) were analyzed using QIAGEN's Ingenuity® Pathway Analysis (IPA®, QIAGEN) and gene set enrichment analysis (GSEA). By default, the false discovery rate (FDR) less than 0.25 is significant in GSEA.

ATAC-seq

ATAC-seq was performed as previously described (16). ATAC libraries were sequenced on an Illumina NextSeq machine (2×75 cycles). The peak sets for ATAC-seq were further analyzed using the deepTools2 suite (v3.3.0)(17). By using bamCoverage, peaks were normalized to reads per kilobase per million reads normalized read numbers (RPKM).

ChIP-seq

ChIP-seq was performed using the ChIP-IT High Sensitivity kit (Active Motif, cat. 53040) as described previously (16). Briefly, formaldehyde (1%, 15 min) fixed cells were sheared to achieve chromatin fragmented to a range of 200–700 bp using an Active Motif EpiShear Probe Sonicator. IMR32 cells were sonicated at 25% amplitude, pulse for 20 sec on and 30 sec off for a total sonication "on" time of 16 min. Sheared chromatin samples were immunoprecipitated overnight at 4 °C with antibodies targeting different proteins (Table S3). To normalize ChIP-seq signal, we employed Active Motif ChIP-seq spike-in using *Drosophila* chromatin (Active Motif catalogue # 53083) and an antibody against *Drosophila* specific histone variant H2Av (Active Motif, catalogue # 61686) according to the manufacturer's instructions. ChIP-seq DNA libraries were prepared by Frederick National Laboratory for Cancer Research sequencing facility. Libraries were multiplexed and sequenced using TruSeq ChIP Samples Prep Kit (75 cycles), cat. # IP-2-2-1012/1024 on an Illumina NextSeq machine.

ChIP-seq data processing

ChIP-seq data processing was performed as described previously (16). Peaks from ChIP-seq of MYCN, HAND2, PHOX2B, GATA3, H3K27ac, H3K4me3, H3K27me3 and RNA Pol II were selected at a stringent p-value ($p<10^{-5}$ for PHOX2B and $p<10^{-7}$ for the rest of the targets). Peaks within 1,000 bp to the nearest TSS were set as promoter. The distribution of peaks (as intronic, intergenic, exonic, etc.) was annotated using HOMER. Enrichment of known and *de novo* motifs were found using HOMER script "find Motifs Genome.pl" (RRID:SCR_010881). Reference genome normalization (RRPM, reference-adjusted reads per million mapped reads) was calculated with the ChIP-Rx method (18).

Monitoring of synergistic effects of drug combinations

The therapeutic effect of Aurora kinase A inhibitor (AURKAi) alisertib (MedChem Express, HY-10971) and HDACs inhibitor (HDACi) LBH589 (Medchem express, HY-10224) in NB cell lines was determined in a checkerboard fashion. Cell lines were seeded in two 96-well plates and incubated overnight. Each combination dose had 2 replications. Next day, cell lines were treated with different dose combination of alisertib and LBH589. Control cells were treated with DMSO. Each plate has their control cells. Cell viability was determined after 72 h using the CellTiter-Glo® luminescent assay (Promega, catalog number G9242). Cell viabilities of DMSO-treated cells were set to 100%. Results were graphed with GraphPad Prism (RRID:SCR_002798) software. IncuCyte® cell confluence assay was used for testing the impact of synergistic effects of drug combinations to NB cell growth in realtime. Representative data from biological replicates were shown in this study.

Xenograft Tumor Studies

To test the therapeutic effect of alisertib and LBH589 *in vivo*, 4–6 weeks old female athymic nude mice (Frederick Animal Facility, NCI) were orthotopically injected (injected through the adrenal fat pad into the adrenal gland) with 2.5×10^5 IMR5-GFP-Luc cells into the in 30 μl Matrigel. Two weeks later, the luminescence signal in the tumor cells was measured by *in vivo* imaging system (IVIS) imaging. When the luminescence signal $>1 \times 10^8$, mice were grouped into 4 groups (10–11 mice/group): Group 1, treated with Vehicle; Group 2, treated with 10 mg/kg alisertib (disserved with 10% DMSO, 40% PEG300, 5% TWEEN-80, 45% saline) by oral gavage twice a day for 7 consecutive days (cycle days 1–7) in a 21-day cycle; Group 3, treated with 3 mg/kg LBH589 (disserved with 15% DMSO and saline) by intraperitoneal injection three times (M-W-F) a week; Group 4, treated with 10 mg/kg alisertib and 3 mg/kg LBH589. After 6 weeks (2 cycles) of drug treatment, mice were euthanized, and tumors were collected and weighed. For the pharmacodynamics (PD) study, when the luminescence signal reached 1×10^8 total flux [p/s], mice were grouped into 4 groups, which were treated with vehicle, alisertib, LBH589 and alisertib + LBH589, respectively. alisertib (10 mg/kg) was given at time 0 h, 8 h and 24 h, LBH589 (3 mg/kg) was given at time 0 h and 24 h. Mice were euthanized 4 h after the final treatment and tumors were collected for western blot analysis. All Xenograft studies were approved by the National Cancer Institute's Animal Care and Use Committee (ACUC), and all animal care was in accordance with institutional guidelines.

Data availability

All the home generated RNA-seq, ChIP-seq and ATAC-seq datasets can be found in the Gene Expression Omnibus (GEO) (RRID:SCR_005012) database. GEO accession number for data generated in this study is GSE183641, and the subseries that are linked to GSE183641 are GSE183609 and GSE183636 for RNA-seq, GSE184057, GSE184058 and GSE184059 for ChIP-seq, GSE184229 and GSE184232 for ATAC-seq. GEO accession number for publicly available ChIP-seq data derived from BE2C cells is GSE94822.

Statistical analysis

The statistical analyses used throughout this paper are specified in the appropriate results paragraphs and Methods sections. Additional statistical analyses were performed using standard two-tailed Student's *t*-test, one-way ANOVA, and the software GraphPad Prism 8.1.0.

RESULTS

CRC TF HAND2 regulates the expression of *MYCN* targets and is essential in NB

We analyzed the published ChIP-seq data of NB CRC TFs and MYCN in the SK-N-BE(2)C (BE(2)C) cell line (*MYCN* amplified) (10) through the Intervene tool (19), and identified both unique and overlapping binding sites among these TFs (Figure 1A). For example, signal tracks showed different combinatorial co-localization among these TFs on genomic loci near the *GATA2* gene locus (Figure 1B).

To determine the biological function of the CRC TFs in NB, we mined the Project Achilles genome-wide CRISPR-Cas9 screen data. We found that compared to other pediatric cancer cell lines, NB cell lines in particular are preferentially dependent on these TFs (Figure S1A), which is consistent with the essential role of CRC TFs previously identified in NB (8–11). We silenced each of these TFs using two different small interference RNAs (siRNAs) (Figure 1C, Figure S1B) and found that the more effective knockdown resulted in a greater decrease in cell number (Figure 1D, Figure S1C). Usually, silencing of one CRC member resulted in a decreased expression of other CRC members (Figure S1D).

We picked five well-known MYCN direct target genes and performed realtime PCR to investigate how MYCN targets were regulated by each of these CRC TFs. Results showed the transcriptional activity of HAND2 most closely phenocopied loss of MYCN (Figure 1E). Silencing of *HAND2* significantly reduced cell viability in all the other tested NB cell lines albeit to varying levels (Figure 1F,G). To confirm that this biological function was not due to an off-target effect of si*HAND2_3*, we performed a *HAND2* rescue experiment by overexpressing a si*HAND2_3* resistant *HAND2* mutant construct (see methods). The overexpression of this *HAND2* mutant construct attenuated both the *siHAND2_3*-induced upregulation of *GAP43* mRNA levels and repression of cell proliferation (Figure S1E,F), demonstrating the specificity of *siHAND2_3*. We generated CRISPR-Cas9 inducible IMR32 stable clones, with a control (sgCtrl) or a single guide RNA that targeted *HAND2* gene locus (*sgHAND2*). Dox treatment decreased HAND2 protein levels (Figure S1G), which was accompanied by decreased cell proliferation and colony formation in soft agar (Figure S1H, Figure 1H), indicating a role of HAND2 in NB tumorigenicity.

In NB patient data we did not observe a consistent association between *HAND2* expression levels and the overall survival in two different NB patient data sets (Figure S1I). However, in *MYCN*-amplified NB patient data, we found that high expression of *HAND2* associates with poor overall survival (Figure S1J), suggesting a cooperative role for HAND2 and MYCN.

HAND2 regulates chromosome accessibility and facilitates MYCN enhancer invasion

To determine whether HAND2 assists MYCN binding to DNA, we silenced *HAND2* in IMR32 cells and performed ChIP-seq and ATAC-seq. ChIP-seq data analyses showed that 70% of the MYCN binding sites overlapping with HAND2 binding sites are at the active enhancer regions (overlapping with H3K27ac binding sites but outside of the promoter) (Figure 2A). However, almost 50% of the MYCN binding sites that did not overlap with HAND2 binding sites (MYCN unique peaks) were at promoter regions (Figure 2B). HOMER (20) *de novo* motif scan identified low-affinity E-box-like sequences (CANNTG) in the peaks MYCN shared with HAND2, while the MYCN unique peaks contain a high-affinity canonical E-box (CACGTG) (Figure 2A, B). Genomic Regions Enrichment of Annotations Tool (GREAT) (21) gene ontology (GO) analysis revealed genes associated with MYCN and HAND2 overlapping sites are enriched in the regulation of sympathetic nervous system development, while the genes associated with unique MYCN peaks are enriched in RNA processing (Figure 2C, D).

We found that approximately 34% MYCN binding sites at the active enhancers did not overlap with HAND2 binding sites (Figure. 2B), indicating that HAND2 binds to a subset of MYCN-bound enhancers. GO analysis showed that the active enhancers bound by both MYCN and HAND2 associate with genes involved in noradrenergic neuron differentiation (Figure S2A, left panel), while the active enhancers only bound by MYCN associate with chromatin organization and modification (Figure S2A, right panel). Motif scan showed enhancers bound by both MYCN and HAND2 are enriched with low-affinity binding non-canonical E-box, PHOX2B and HAND2 binding motifs (Figure S2B, left panel), while MYCN unique enhancers are enriched with high-affinity canonical E-box but not CRC TFs binding motifs (Figure S2B, right panel). These analyses indicate that the enhancers colocalized by HAND2 and MYCN are selectively more noradrenergic than MYCN-specific enhancers.

We next investigated the influence of HAND2 on MYCN binding to DNA by knocking down *HAND2* in IMR 32 cells (Figure S2C). At the HAND2 and MYCN overlapping binding sites, loss of *HAND2* caused a 40% decrease (summit of the composite plot) in the average MYCN ChIP-seq signal, as well as a 30% decrease in the average ATAC-seq signal, reflecting a decrease of chromatin accessibility (Figure 2E). A representative example within the *CARMN* gene locus is shown by signal tracks (Figure 2F). The depletion of HAND2 was not always accompanied by decreased MYCN binding. Thus, we stratified the ChIP-seq peaks into Group I, those with decreased MYCN ChIP-seq signals (>40% decrease); or Group II, those with no change in MYCN signals after *HAND2* silencing (within ±1.1-fold changes). Analysis of the resulting peaks (heatmap) showed that the loss of *HAND2* decreased MYCN and ATAC-seq signals in Group I regions (Figure S2D). In contrast after *HAND2* knockdown, the Group II regions were not associated with changes in MYCN and ATAC-seq signals (Figure S2D). These results indicate that the removal of both HAND2 and MYCN from DNA is associated with a decrease in chromatin accessibility.

In *HAND2* gain-of-function studies, induction of *HAND2* for 36 h in IMR32 cells did not alter MYCN levels (Figure S2E). The ChIP-seq signal of many of the HAND2 peaks did not increase after the overexpression of HAND2 possibly due to the saturation of endogenous

HAND2 on these genomic loci. Thus, we focused on those HAND2 and MYCN common peaks whose HAND2 ChIP-seq signal increased (>3-fold). On these, a gain of *HAND2* expression increased the average MYCN ChIP-seq and ATAC-seq signals (Figure 2G,H).

We further examined MYCN binding on DNA at 24 h after knocking down *HAND2* in IMR32 cells when there was no change in MYCN protein levels (Figure S2F). By focusing on all the HAND2 and MYCN overlapping binding sites, the loss of *HAND2* resulted in a 5% decrease in the average MYCN ChIP-seq signal at the summit (Figure S2G, left panel). However, for the HAND2 and MYCN overlapping peaks with > 4-fold decrease of HAND2 ChIP-seq signal, there was a 25% decrease of MYCN ChIP-seq signal at the summit (Figure S2G, middle panel). The loss of *HAND2* for 24 h did not affect the MYCN ChIP-seq signal of those MYCN unique peaks that did not overlap with HAND2 binding sites (Figure S2G, right panel). IMR32tetHAND2 cells treated with Dox for 6 h resulted in increases in HAND2 protein levels without affecting MYCN expression (Figure S2H). Yet the overexpression of *HAND2* for 6 h resulted in a significant increase of the average MYCN ChIP-seq signal at HAND2 peak center with HAND2 signals increasing by 3 to 4-fold (Figure S2I,J). Representative signal tracks close to *TBX4* or *UQCRFS1* gene locus demonstrated this influence of HAND2 silencing on MYCN binding to DNA in a time-dependent manner (Figure S2K,L).

Using a Dox-inducible MYCN overexpression IMR32 stable cell line, we found that over expressing MYCN did not rescue the decrease in cell proliferation induced by *HAND2*-silencing (Figure S2M,N). Next, we performed MYCN ChIP-seq analysis in *MYCN*-overexpressed IMR32 cells before and after the silencing of *HAND2* and found that *HAND2* depletion caused a 30% decrease in the average MYCN ChIP-seq signal at the summit (Figure S2O). Thus, HAND2 is required to recruit MYCN to chromatin and the overexpression of *MYCN* cannot fully rescue the effect of silencing *HAND2*.

HAND2, PHOX2B and GATA3 are broadly identified as CRC TFs in tested NB cell lines (8–10). Next, we investigated how HAND2 silencing affects the PHOX2B and GATA3 binding to MYCN regulated genes. The silencing of *HAND2* for 72 h resulted in a >20% decrease in GATA3 protein levels but did not alter PHOX2B expression (Figure S2P). Composite plots at the HAND2 and MYCN overlapping binding sites showed decreases in average GATA3 but not PHOX2B ChIP-seq signals after silencing *HAND2* (Figure 2I). Decreases in GATA3 ChIP-seq signal might partially be due to decreases in GATA3 protein levels caused by *HAND2* silencing (Figure S2P). Nevertheless, the depletion of HAND2 results in decreases in DNA-bound MYCN and GATA3 but not PHOX2B, suggesting a complicated cooperative gene regulatory network.

To investigate whether PHOX2B and GATA3 are required for MYCN to bind to DNA, we silenced their expression in IMR32 cells and performed ChIP-seq and ATAC-seq experiments. Western blot results showed that *PHOX2B* silencing for 72 h did not affect MYCN protein levels (Figure S2Q) while *GATA3* silencing resulted in an increase in MYCN protein levels (Figure S2R). The composite plots showed that the average ChIP-seq signal of MYCN did not change after *PHOX2B* silencing (Figure 2J), while the *GATA3* silencing increased MYCN ChIP-seq signal (Figure 2K), which might be due to increases

in MYCN protein after *GATA3* silencing (Figure S2R). Our results indicate that CRC TF HAND2, but not PHOX2B or GATA3 is required for MYCN to bind to DNA.

Next, we investigated how *MYCN* silencing affects the CRC TFs-DNA interactions. Knockdown of *MYCN* for 72 h increased GATA3 protein levels but not the other TFs (Figure S2S). Composite plots showed that *MYCN* silencing led to decreases in MYCN ChIP-seq signal but not HAND2 binding (Figure S2T). By focusing on GATA3 and PHOX2B, we found that depletion of MYCN resulted in increases in GATA3 and PHOX2B ChIP-seq signals (Figure S2U,V).

To determine whether HAND2 facilitates MYCN DNA binding and increases chromatin accessibility is cell line specific, we analyzed LAN5 NB cells. *HAND2* silencing for 72 h resulted in a 17% decrease in MYCN protein (Figure S2W) with a 30% decrease in the average MYCN ChIP-seq signal at the summit of the composite plots (Figure S2X). Only a 5% decrease in the average ATAC-seq signal was observed (Figure S2X). In IMR32 cells only when both HAND2 and MYCN were absent from DNA, there was an obvious decrease of chromatin accessibility as indicated by decreases in ATAC-seq signal (Figure S2D). Thus, we specifically focused on those HAND2 and MYCN overlapped binding sites with a >1.5-fold decrease of MYCN ChIP-seq signal after HAND2 depletion in LAN5 cells. Remarkably, composite plots showed an approximately 50% decrease in ATAC-seq signal at summit when both HAND2 and MYCN were absent from DNA upon HAND2 silencing (Figure S2Y). These results indicate that HAND2 facilitates MYCN enhancer binding, and the cooperative-binding of these TFs on DNA is associated with increased chromatin accessibility.

HAND2 regulates the expression of a subset of *MYCN* target genes

To investigate the global gene expression regulated by HAND2 or MYCN, we performed RNA-seq in *HAND2 or MYCN* silenced IMR32 cells (Figure S2C). Gene set enrichment analysis (GSEA) of the RNA-seq data showed that loss of *HAND2* resulted in a significant negative enrichment of MYC targets and positive enrichment of neuronal gene signatures (Figure 3A). Around 44% of the genes regulated by MYCN were also regulated by HAND2 (Figure 3B, Table S4). In LAN5 cells, *HAND2* silencing (Figure S2W) resulted in a significant negative enrichment of MYC targets and positive enrichment of neuronal gene signatures (Figure 3C). Around 33% of the genes regulated by MYCN were also regulated by HAND2 (Figure 3D, Table S5). *HAND2* silencing resulted in a positive enrichment of neuronal genes and increased functional neuronal differentiation as shown by neurite extension in both IMR32 cells and LAN5 cells (Figure S3A,B). We found that among the 216 genes regulated by both MYCN and HAND2 in LAN-5 cells, 46 neuronal-enriched genes were also regulated by both MYCN and HAND2 in IMR32 cells (Table S5).

Loss of *HAND2* affects regional epigenetic modifications

To investigate how HAND2 regulates gene transcription at the epigenetic levels, we silenced *HAND2* in IMR32 cells and performed ATAC-seq and ChIP-seq for histone marks, RNA Pol II, RNA Pol II Ser2P (S2), and BRD4. Analysis of HAND2 ChIP-seq identified 25549 high-confidence HAND2 binding sites in the IMR32 cells that aligned with or without those

transcriptional marks shown in the heatmaps (Figure 4A). GREAT analysis of HAND2 binding sites showed that the majority of HAND2 binding sites were distal (>5 kb) to the transcription start site (TSS) (Figure 4B). Peak distribution analysis showed that 46% of HAND2-binding sites were at the active enhancer regions (overlapped with H3K27ac peaks) (Figure 4C). Homer *de novo* motif scanning of HAND2 peaks identified two highly enriched known HAND2 binding motifs (Figure 4D) identified in NB (8) or in human embryonic stem cell derived mesoderm cells (GSE61475). GO analysis showed HAND2 peak-associated genes were enriched in sympathetic nervous system development (Figure 4E).

ChIP-seq and ATAC-seq heatmaps demonstrated that most of the ranked HAND2-centered peaks identified in siCtrl IMR32 cells aligned with the H3K27ac, RNA Pol II peaks and ATAC-seq peaks (Figure 4A), indicating that most HAND2 binding sites are within accessible chromatin regions. No H3K27me3 signal and weak H3K4me3 signal were detected at the HAND2 peak center (Figure 4A), both of which were known to be restricted from enhancer regions. Silencing of *HAND2* resulted in an almost complete loss of HAND2 signal that was accompanied by decreases in H3K27ac signal at the HAND2 peak center, while no obvious decrease of average BRD4 ChIP-seq signal was observed (Figure 4A). Co-immunoprecipitation using anti-HAND2 antibody indicated that HAND2 did not pull down BRD4 (Figure S4A). These results suggest that BRD4 does not mediate HAND2 function at facilitating MYCN enhancer invasion or increasing chromatin accessibility.

As a component of the CRC, HAND2 is driven by super-enhancers (SEs) and binds to the SEs of genes important for cell-identity (8,10). However, whether HAND2 plays a role in the establishment of SEs has not been investigated. We identified 409 SEs (associated with 355 genes) in *siCtrl* and 439 SEs (associated with 382 genes) in *siHAND2* cells (Figure 4F). The loss of *HAND2* resulted in a loss of 87 SEs associated genes and an acquisition of 114 SEs associated genes with 267 SEs associated genes relatively unchanged (Table S6). Representative ChIP-seq signal tracks showed that *HAND2* silencing resulted in a dramatic decrease of H3K27ac and RNA-seq signals at the *HAND1* gene locus (Figure 4G), and a dramatic increase of H3K27ac and RNA-seq signals at the *CNTN2* gene locus (Figure S4B).

To investigate how HAND2 regulates gene transcription, we focused on genes with HAND2 binding sites that were transcriptionally regulated by HAND2. In combination with HAND2 ChIP-seq and RNA-seq results, we identified 605 directly down-regulated genes (associate with 2065 peaks) and 464 directly up-regulated genes (associate with 1890 peaks) after *HAND2* silencing (Table S7). By focusing on the directly “down-regulated genes” after *HAND2* silencing, the composite plots showed that the average H3K27ac signal decreased upon HAND2 silencing (Figure 4H). Decreased H3K27ac but not H3K4me3 and H3K27me3 signals occurred at TSS (Figure 4H), and decreased signals for RNA Pol II Ser2P but not RNA Pol II occurred both within the gene bodies and in the regions downstream of the poly-adenylation signals (Figure 4H, Figure S4C). Pathway analysis of these “down-regulated genes” indicated that *HAND2* silencing activated PTEN signaling (Figure S4D). For genes directly “up-regulated” after *HAND2* silencing, the composite plots showed no change for H3K27ac signal at HAND2 peak centers, but increased H3K27ac and H3K4me3 signals, and decreased H3K27me3 signal were observed at TSS (Figure

4I). Increased RNA Pol II and RNA Pol II Ser2P signals in the region downstream of the poly-adenylation signals were observed (Figure 4I, Figure S4E). Pathway analysis of genes up-regulated after *HAND2* silencing (HAND2 repressed genes) showed that these genes were associated with activated neuronal development related signaling (Figure S4F). Our results suggest that HAND2 activates gene transcription mainly by increasing enhancer activity, while HAND2 represses gene transcription mainly by decreasing promoter activity.

HAND2 and MYCN work together to cooperatively regulate chromatin accessibility

The "*cooperative*" TF-DNA binding model proposes that the TFs recognize adjacent binding sites and work together to compete with a nucleosome to access and cooperatively bind DNA (22–24). If HAND2 and MYCN cooperate in this way, the loss of both *HAND2* and *MYCN* should have a dramatic effect on nucleosome occupancy. To test this both *HAND2* and *MYCN* were silenced (Figure S5A), and ATAC-seq for chromatin accessibility was assessed. By focusing on the MYCN and HAND2 common binding sites, we stratified the ChIP-seq peaks into Group I, those that had a decreased MYCN ChIP-seq signal (>1.5-fold change); or Group II in which there was no change of ChIP-seq signal (<1.1-fold change) in the MYCN signal after the silencing of *HAND2*. Analysis of the resulting peaks (heatmap) showed that the loss of *HAND2* decreased MYCN binding and was accompanied by a decrease in the ATAC-seq signal in Group I regions (Figure 5A, left panel). In contrast after *HAND2* knockdown, the Group II regions were not associated with changes in MYCN binding or average ATAC-seq signal (shown in the heatmap, Figure 5A, left panel). The same results were also shown in composite plots (Figure 5A, right panel). The knockdown of both *HAND2* and *MYCN* led to greater decreases in chromatin accessibility shown by the decreased ATAC-seq signal in both heatmaps and composite plots (Figure 5A). We specifically focused on those HAND2 and MYCN common peaks in which there were no changes in MYCN binding and ATAC-seq signal after silencing *HAND2* alone (Figure 5A, Group II). In these genomic regions, we found that the knockdown of either *HAND2* or *MYCN* alone had no effect on chromatin accessibility. It was only the loss of both *HAND2* and *MYCN* that decreased chromatin accessibility as detected by the decreased ATAC-seq signal (Figure 5A).

GO analysis of Group I MYCN peaks (Figure 5A) associated genes showed that these genes are dominantly enriched in nervous system development, while Group II MYCN peaks (Figure 5A) associated genes are enriched in both nervous system development and heart development (Figure S5B,C). Both HAND2 and MYCN have been reported to be essential in regulating heart development (25,26). These results indicate that although these TFs bind to heart development associated genes in NB, the depletion of *HAND2* only affects MYCN binding on neuronal genes but not cardiac genes. Motif scan showed some difference in the motifs enriched in Group I and II (Figure S5D,E). HAND2 is known to bind to the non-canonical E-box, as well as a thymine (T) nucleotide enriched motif. In Group I but not Group II, we observed an enrichment of T nucleotide enriched HAND2 binding motif, which suggests that this special HAND2-DNA binding facilitates MYCN to bind to DNA sites of Group I.

Taken together, these results show that HAND2 cooperates with MYCN to increase chromatin accessibility of neuronal genes in NB most probably by competing with nucleosomes to access and bind DNA.

HAND2 and MYCN cooperatively regulate gene transcription

To determine the effect of the loss of both *HAND2* and *MYCN* on global gene transcriptional regulation, we performed RNA-seq analysis. The silencing of both *HAND2* and *MYCN* in IMR32 cells led to greater changes in gene expression when compared with the silencing of either *HAND2* or *MYCN* alone (Figure S5F, Figure 5B left panel, Table S8). Pathway analysis showed that the knockdown of both *HAND2* and *MYCN* decreased transcription of the “mitotic signaling” pathway and activation of transcription in the “G2/M checkpoint regulation” (Figure 5B right panel). GSEA showed that the combined knockdown of both *HAND2* and *MYCN* resulted in a negative enrichment of *MYC* signature genes, and a positive enrichment of neuronal markers (Figure 5C–F). Consistent with the dramatic epigenome and transcriptome changes resulting from the silencing of both *HAND2* and *MYCN* expression, the loss of both TFs compared with loss of either one alone led to increased functional neuronal differentiation (Figure 5G,H).

Targeting both MYCN and the CRC TFs is effective in suppressing NB tumor growth

We found that MYCN and HAND2 cooperatively bind to DNA to regulate gene transcription and determine a malignant NB phenotype, suggesting that targeting both MYCN and HAND2 simultaneously using small molecules will be more effective in suppressing NB growth. Thus, we investigated the effect of pharmacologically targeting both MYCN and CRC TFs including HAND2. As a proof of concept, here we selected the Aurora A kinase inhibitor (AURKAi) alisertib to target MYCN, and the HDAC inhibitor (HDACi) LBH589 to target CRC TFs. AURKA interacts with both MYCN and the SCF ubiquitin ligase to stabilize MYCN protein resulting in AURKAi treatment that increases the degradation of MYCN in NB cells (27,28). Since super-enhancers (SEs) often drive oncogenes in cancers and CRC components are found to be essential in cancers, we chose a HDAC inhibitor (HDACi) that was known to disrupt SE-driven CRCs (10,29–32).

We found that the treatment of NB cells with alisertib and LBH589 was more effective in reducing the viable cell number in *MYCN*-amplified cell lines compared to *MYCN* single-copy NB cell lines (Figure 6A, Figure S6A). Half-maximal inhibitory concentration (IC50) assays clearly showed that *MYCN*-amplified cell lines were more sensitive to the LBH589 and alisertib, with IC50 values averaging greater than 4x lower than those found in *MYCN* single-copy cell lines (Figure S6B). These results indicated potent and selective effects of both HDACi and AUKRAi in *MYCN*-dysregulated cells. Importantly, the combination treatment using alisertib and LBH589 synergistically reduced viable NB cell numbers with average bliss synergy scores greater than 10 across a range of doses in IMR32, IMR5 or KCNR cells (Figure 6B). Cell confluence assays confirmed the synergistic effects of alisertib + LBH589 treatment on cell proliferation in *MYCN*-amplified NB cell lines (Figure 6C). As expected, 6 h of HDACi LBH589 treatment resulted in a decrease of the SE-driven CRC components *HAND2*, *PHOX2B* and *GATA3* at the mRNA levels in all the tested NB cell lines (Figure S6C). As previously reported the inhibition of AURKA destabilized

MYCN (27,28), we found that a 48 h alisertib treatment resulted in a 30–50% decrease of MYCN at protein levels in NB cells compared to control (Figure 6D). Although the effect was TF and cell-line dependent, LBH589 treatment decreased both MYCN and CRC TF protein levels compared with the control, with decreases approaching 50% in most cell lines evaluated (Figure 6D). The combination of alisertib and LBH589 treatment caused a ~80% decrease in MYCN and the CRC TFs protein levels after 48 h treatment in all the tested cell lines (Figure 6D), indicating that this combined treatment was far more potent at inhibiting these targets than single agent treatment.

Next, we evaluated the activity of alisertib combined with LBH589 in preclinical NB xenograft models. Our pilot study showed that the tumor incidence of IMR32 implanted athymic nude mice was 67.6% (23 out of 34) with a tumor size variance of 147.4 ± 151.8 (mm^3) after two months. Thus, the IMR32 cell line is not a reliable *in vivo* model for reproducibility issues. For this reason we used IMR32 subclone IMR5 (33), as these two cell lines had a similar response to the treatment of alisertib plus LBH589 *in vitro* (Figure 6A–D). IMR5 cells stably expressing GFP-Luc were injected at the orthotopic site of the nude mouse. Animals were randomized according to their bioluminescence signal and received therapy with two treatment cycles of drug treatment (Figure 6E) (see materials and methods). Although protein levels of MYCN and CRC components in collected tumors were heterogeneous, the overall levels of these proteins were lower in the drug treatment groups compared with the vehicle treatment group (Figure S6D). Increased H3K27ac signal was observed in the groups of mice treated with either LBH589 alone or LBH589 + alisertib (Figure S6D). Animals across all groups did not exhibit any signs of overt toxicity (Figure S6E). Importantly, tumor weight (Figure 6F) measurements revealed that the combination of alisertib and LBH589 treatment was superior to either single agent alone at suppressing tumor growth. Our results demonstrated that the combination therapy of alisertib + LBH589 was effective in *MYCN*-amplified NB.

DISCUSSION

Combinatorial control of gene expression by a small group of TFs is critical to establish and maintain the cancer cell identity (13,24,34). In this study, we identify that the CRC TF HAND2 assists MYCN in enhancer binding, and that these two TFs compete with nucleosomes to cooperatively regulate global gene expression. By targeting both MYCN and the NB CRC we find that a combination of AURKAi and HDACi treatment of NB cells more potently reduces the protein levels of both MYCN and CRC TFs than the treatment of NB cells with each drug alone, which results in a more effective inhibition of NB tumor growth (Figure 7).

Our study shows that HAND2 selectively influences MYCN-enhancer binding as the loss of *HAND2* results in a decrease in genome bound MYCN while the overexpression of *HAND2* leads to an increase in genome bound MYCN. HAND2, PHOX2B and GATA3 are highly expressed in NB and form a CRC to cooperate with MYCN to determine a noradrenergic NB phenotype (10). Here we find that the loss of HAND2 but not PHOX2B or GATA3 decreases MYCN enhancer binding at the genome-wide level. We find that HAND2 assists MYCN in binding to a majority of MYCN-bound enhancers, but other TFs might

be required for MYCN to bind to the other genomic loci. CRISPR-Cas9 screen of NB cell lines indicates that HAND2 is essential in both *MYCN* single copy and *MYCN*-amplified NB cell lines (Figure S1A). One reason is that MYCN protein expression might be high in some of the NB cell lines without MYCN amplification (35). Another explanation is that HAND2 has MYCN independent function as greater than 50% of HAND2 regulated genes are not regulated by MYCN (Figure 3B,D). Nevertheless, the simultaneous silencing of both *HAND2* and *MYCN* in NB cells results in greater changes in gene expression when compared with the silencing of either *HAND2* or *MYCN* alone. This further demonstrates that these two TFs cooperatively regulate global gene expression.

Our results suggest that HAND2 facilitates MYCN enhancer invasion via a "*cooperative*" TFs-DNA binding model. In this TFs-DNA binding model, TFs recognize adjacent binding sites within regulatory regions to compete with nucleosomes to gain access and bind DNA simultaneously or sequentially (22–24,36,37). Our ATAC-seq results show that the silencing of both *HAND2* and *MYCN* results in a more dramatic decrease of chromatin accessibility than the silencing of either TF alone. These results indicate that HAND2 and MYCN cooperate to compete with nucleosomes and achieve specific DNA binding. This cooperativity may arise with the assistance of ATP-dependent nucleosome remodeling factors. For example, initially bound TF recruits a remodeler to disassemble or move a nucleosome to facilitate binding of a second TF towards its binding site (20). We did not identify chromatin remodelers that are regulated by HAND2 at the mRNA level based on RNA-seq data analysis. We have tested BRD4, which is known to enhance chromatin accessibility (38), but find that it does not mediate HAND2 function at regulating chromatin accessibility. Additional chromatin remodelers will be evaluated to determine how the loss of HAND2 leads to changes in chromatin accessibility in our future studies.

SEs often drive the expression of oncogenes and CRC components in cancers (10,31) and the Bromo-domain inhibitor JQ1 causes transcriptional repression of SE associated oncogenes (39). Recent studies showed that the combination of JQ1 and CDK7 inhibitor THZ1 reduced the expression of MYCN and CRC components and synergistically suppressed NB growth (10,11). Here we take a different approach to target these TFs by using clinically-relevant AURKA and HDAC inhibitors (40,41). AURKA inhibitor (AURKAi) treatment increases degradation of MYCN in NB cells (27,28). HDAC inhibitor (HDACi) treatment of cancer cells spreads hyperacetylated histones and disrupts the three-dimensional (3D) organization of SEs, thereby destabilizing CRC TFs and RNA Pol II binding at SEs and selectively suppresses CRC TF transcription (29,30,32). As expected, we find that the combination of AURKAi and HDACi treatment of NB cells reduces expression of both MYCN and CRC TFs and synergistically suppresses NB cell proliferation in MYCN-amplified cells.

The finding that the CRC component HAND2 assists oncogenic protein MYCN to bind to DNA enhancer regions adds another layer to our understanding of how CRC TFs form a combinatorial transcriptional regulatory circuit to determine cell identity in this disease state. Our finding provides a rationale for targeting multiple TFs simultaneously to increase the disruption of this "combinatorial transcription regulatory network" in cancer cells and improve therapeutic efficacy.

Supplementary Material

Refer to Web version on PubMed Central for supplementary material.

ACKNOWLEDGEMENTS

This work was funded by the Center for Cancer Research, Intramural Research Program at the National Cancer Institute. We thank Bao Tran, Jyoti Shetty and Yongmei Zhao from NCI Sequencing Facility for DNA and RNA sequencing. This work utilized the computational resources of the NIH HPC Biowulf cluster (http://hpc.nih.gov). The graphical abstract was created with BioRender.com.

REFERENCE

1. Lambert SA, Jolma A, Campitelli LF, Das PK, Yin Y, Albu M, et al. The Human Transcription Factors. Cell 2018;172:650–65 [PubMed: 29425488]
2. Meyer N, Penn LZ. Reflecting on 25 years with MYC. Nat Rev Cancer 2008;8:976–90 [PubMed: 19029958]
3. Sabo A, Kress TR, Pelizzola M, de Pretis S, Gorski MM, Tesi A, et al. Selective transcriptional regulation by Myc in cellular growth control and lymphomagenesis. Nature 2014;511:488–92 [PubMed: 25043028]
4. Lin CY, Loven J, Rahl PB, Paranal RM, Burge CB, Bradner JE, et al. Transcriptional amplification in tumor cells with elevated c-Myc. Cell 2012;151:56–67 [PubMed: 23021215]
5. Zeid R, Lawlor MA, Poon E, Reyes JM, Fulciniti M, Lopez MA, et al. Enhancer invasion shapes MYCN-dependent transcriptional amplification in neuroblastoma. Nat Genet 2018;50:515–23 [PubMed: 29379199]
6. Matthay KK, Maris JM, Schleiermacher G, Nakagawara A, Mackall CL, Diller L, et al. Neuroblastoma. Nat Rev Dis Primers 2016;2:16078 [PubMed: 27830764]
7. Cheung NK, Dyer MA. Neuroblastoma: developmental biology, cancer genomics and immunotherapy. Nat Rev Cancer 2013;13:397–411 [PubMed: 23702928]
8. Boeva V, Louis-Brennetot C, Peltier A, Durand S, Pierre-Eugene C, Raynal V, et al. Heterogeneity of neuroblastoma cell identity defined by transcriptional circuitries. Nat Genet 2017;49:1408–13 [PubMed: 28740262]
9. van Groningen T, Koster J, Valentijn LJ, Zwijnenburg DA, Akogul N, Hasselt NE, et al. Neuroblastoma is composed of two super-enhancer-associated differentiation states. Nat Genet 2017;49:1261–6 [PubMed: 28650485]
10. Durbin AD, Zimmerman MW, Dharia NV, Abraham BJ, Iniguez AB, Weichert-Leahey N, et al. Selective gene dependencies in MYCN-amplified neuroblastoma include the core transcriptional regulatory circuitry. Nat Genet 2018;50:1240–6 [PubMed: 30127528]
11. Decaesteker B, Denecker G, Van Neste C, Dolman EM, Van Loocke W, Gartlgruber M, et al. TBX2 is a neuroblastoma core regulatory circuitry component enhancing MYCN/FOXM1 reactivation of DREAM targets. Nat Commun 2018;9:4866 [PubMed: 30451831]
12. Wang L, Tan TK, Durbin AD, Zimmerman MW, Abraham BJ, Tan SH, et al. ASCL1 is a MYCN- and LMO1-dependent member of the adrenergic neuroblastoma core regulatory circuitry. Nat Commun 2019;10:5622 [PubMed: 31819055]
13. Bradner JE, Hnisz D, Young RA. Transcriptional Addiction in Cancer. Cell 2017;168:629–43 [PubMed: 28187285]
14. Liu Z, Yang X, Tan F, Cullion K, Thiele CJ. Molecular cloning and characterization of human Castor, a novel human gene upregulated during cell differentiation. Biochem Biophys Res Commun 2006;344:834–44 [PubMed: 16631614]
15. Liu Z, Lam N, Wang E, Virden RA, Pawel B, Attiyeh EF, et al. Identification of CASZ1 NES reveals potential mechanisms for loss of CASZ1 tumor suppressor activity in neuroblastoma. Oncogene 2017;36:97–109 [PubMed: 27270431]

16. Liu Z, Zhang X, Lei H, Lam N, Carter S, Yockey O, et al. CASZ1 induces skeletal muscle and rhabdomyosarcoma differentiation through a feed-forward loop with MYOD and MYOG. Nat Commun 2020;11:911 [PubMed: 32060262]
17. Ramirez F, Ryan DP, Gruning B, Bhardwaj V, Kilpert F, Richter AS, et al. deepTools2: a next generation web server for deep-sequencing data analysis. Nucleic Acids Res 2016;44:W160–5 [PubMed: 27079975]
18. Orlando DA, Chen MW, Brown VE, Solanki S, Choi YJ, Olson ER, et al. Quantitative ChIP-Seq normalization reveals global modulation of the epigenome. Cell Rep 2014;9:1163–70 [PubMed: 25437568]
19. Khan A, Mathelier A. Intervene: a tool for intersection and visualization of multiple gene or genomic region sets. BMC Bioinformatics 2017;18:287 [PubMed: 28569135]
20. Heinz S, Benner C, Spann N, Bertolino E, Lin YC, Laslo P, et al. Simple combinations of lineage-determining transcription factors prime cis-regulatory elements required for macrophage and B cell identities. Mol Cell 2010;38:576–89 [PubMed: 20513432]
21. McLean CY, Bristor D, Hiller M, Clarke SL, Schaar BT, Lowe CB, et al. GREAT improves functional interpretation of cis-regulatory regions. Nat Biotechnol 2010;28:495–501 [PubMed: 20436461]
22. Moyle-Heyrman G, Tims HS, Widom J. Structural constraints in collaborative competition of transcription factors against the nucleosome. J Mol Biol 2011;412:634–46 [PubMed: 21821044]
23. Mirny LA. Nucleosome-mediated cooperativity between transcription factors. Proc Natl Acad Sci U S A 2010;107:22534–9 [PubMed: 21149679]
24. Reiter F, Wienerroither S, Stark A. Combinatorial function of transcription factors and cofactors. Curr Opin Genet Dev 2017;43:73–81 [PubMed: 28110180]
25. George RM, Firulli AB. Hand Factors in Cardiac Development. Anat Rec (Hoboken) 2019;302:101–7 [PubMed: 30288953]
26. Harmelink C, Peng Y, DeBenedittis P, Chen H, Shou W, Jiao K. Myocardial Mycn is essential for mouse ventricular wall morphogenesis. Dev Biol 2013;373:53–63 [PubMed: 23063798]
27. Brockmann M, Poon E, Berry T, Carstensen A, Deubzer HE, Rycak L, et al. Small molecule inhibitors of aurora-a induce proteasomal degradation of N-myc in childhood neuroblastoma. Cancer Cell 2013;24:75–89 [PubMed: 23792191]
28. Otto T, Horn S, Brockmann M, Eilers U, Schuttrumpf L, Popov N, et al. Stabilization of N-Myc is a critical function of Aurora A in human neuroblastoma. Cancer Cell 2009;15:67–78 [PubMed: 19111882]
29. Sanchez GJ, Richmond PA, Bunker EN, Karman SS, Azofeifa J, Garnett AT, et al. Genome-wide dose-dependent inhibition of histone deacetylases studies reveal their roles in enhancer remodeling and suppression of oncogenic super-enhancers. Nucleic Acids Res 2018;46:1756–76 [PubMed: 29240919]
30. Gryder BE, Wu L, Woldemichael GM, Pomella S, Quinn TR, Park PMC, et al. Chemical genomics reveals histone deacetylases are required for core regulatory transcription. Nat Commun 2019;10:3004 [PubMed: 31285436]
31. Hnisz D, Abraham BJ, Lee TI, Lau A, Saint-Andre V, Sigova AA, et al. Super-enhancers in the control of cell identity and disease. Cell 2013;155:934–47 [PubMed: 24119843]
32. Gryder BE, Pomella S, Sayers C, Wu XS, Song Y, Chiarella AM, et al. Histone hyperacetylation disrupts core gene regulatory architecture in rhabdomyosarcoma. Nat Genet 2019;51:1714–22 [PubMed: 31784732]
33. Bukovsky J, Evans A, Tartaglione M, Kennett RH. Selection of variant neuroblastoma cell line which has lost cell surface expression of antigen detected by monoclonal antibody PI153/3. Somat Cell Mol Genet 1985;11:517–22 [PubMed: 3898405]
34. Bushweller JH. Targeting transcription factors in cancer — from undruggable to reality. Nature Reviews Cancer 2019;19:611–24 [PubMed: 31511663]
35. Valentijn LJ, Koster J, Haneveld F, Aissa RA, van Sluis P, Broekmans ME, et al. Functional MYCN signature predicts outcome of neuroblastoma irrespective of MYCN amplification. Proc Natl Acad Sci U S A 2012;109:19190–5 [PubMed: 23091029]

36. Vashee S, Melcher K, Ding WV, Johnston SA, Kodadek T. Evidence for two modes of cooperative DNA binding in vivo that do not involve direct protein-protein interactions. Curr Biol 1998;8:452–8 [PubMed: 9550700]

37. Miller JA, Widom J. Collaborative competition mechanism for gene activation in vivo. Mol Cell Biol 2003;23:1623–32 [PubMed: 12588982]

38. Devaiah BN, Case-Borden C, Gegonne A, Hsu CH, Chen Q, Meerzaman D, et al. BRD4 is a histone acetyltransferase that evicts nucleosomes from chromatin. Nat Struct Mol Biol 2016;23:540–8 [PubMed: 27159561]

39. Puissant A, Frumm SM, Alexe G, Bassil CF, Qi J, Chanthery YH, et al. Targeting MYCN in neuroblastoma by BET bromodomain inhibition. Cancer Discov 2013;3:308–23 [PubMed: 23430699]

40. Bavetsias V, Linardopoulos S. Aurora Kinase Inhibitors: Current Status and Outlook. Front Oncol 2015;5:278 [PubMed: 26734566]

41. Suraweera A, O'Byrne KJ, Richard DJ. Combination Therapy With Histone Deacetylase Inhibitors (HDACi) for the Treatment of Cancer: Achieving the Full Therapeutic Potential of HDACi. Front Oncol 2018;8:92 [PubMed: 29651407]

Significance statement

HAND2 and MYCN compete with nucleosomes to regulate global gene transcription and drive a malignant neuroblastoma phenotype.

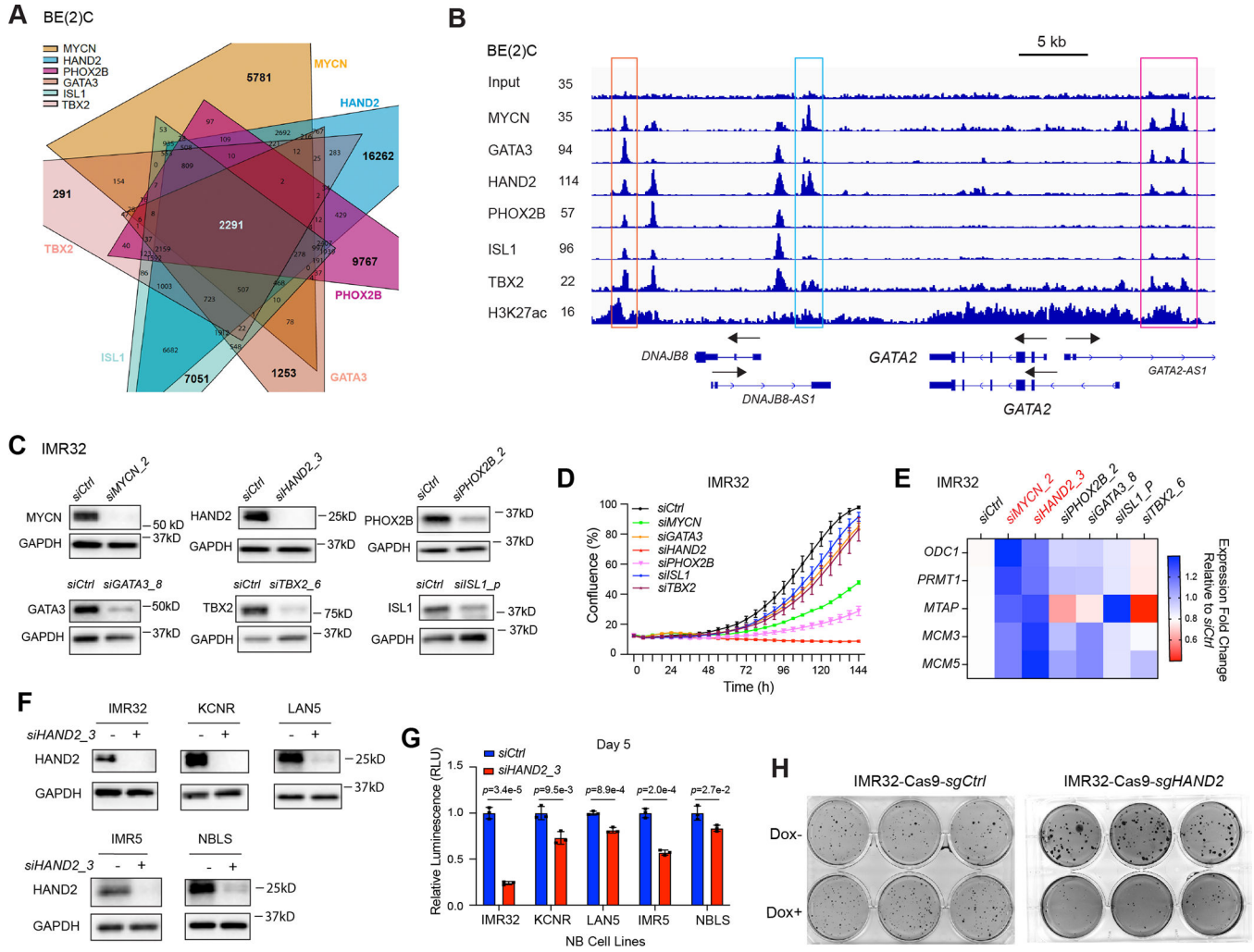

Figure 1. HAND2 regulates the expression of *MYCN* targets and is essential in NB.

(A) Intersection plot shows the overlap of ChIP-seq peaks of CRC TFs and MYCN determined by ChIP-seq data analysis (B) ChIP-seq signal tracks show the overlapped binding sites of CRC TFs and MYCN next to *GATA2* gene locus. (C) The knockdown of each of the CRC TFs for 72 h detected by western blot assay. (D) The knockdown of CRC TFs results in a decrease of cell number shown by the IncuCyte cell confluence assay. (E) The regulation of a panel *MYCN* direct target genes by MYCN and the CRC TFs is detected by realtime PCR and shown in the heatmap after silencing each of these TFs for 72 h. (F) The knockdown of *HAND2* in different NB cell lines for 72 h detected by western blot assay. (G) The effect of silencing of *HAND2* on NB cell proliferation detected by CellTiter-Glo assay. (H) Depletion of *HAND2* through Dox (0.5 μg/ml) inducible Crispr/Cas9 system results in a decrease of anchorage-independent cell growth shown by the reduced colony formation in soft agar.

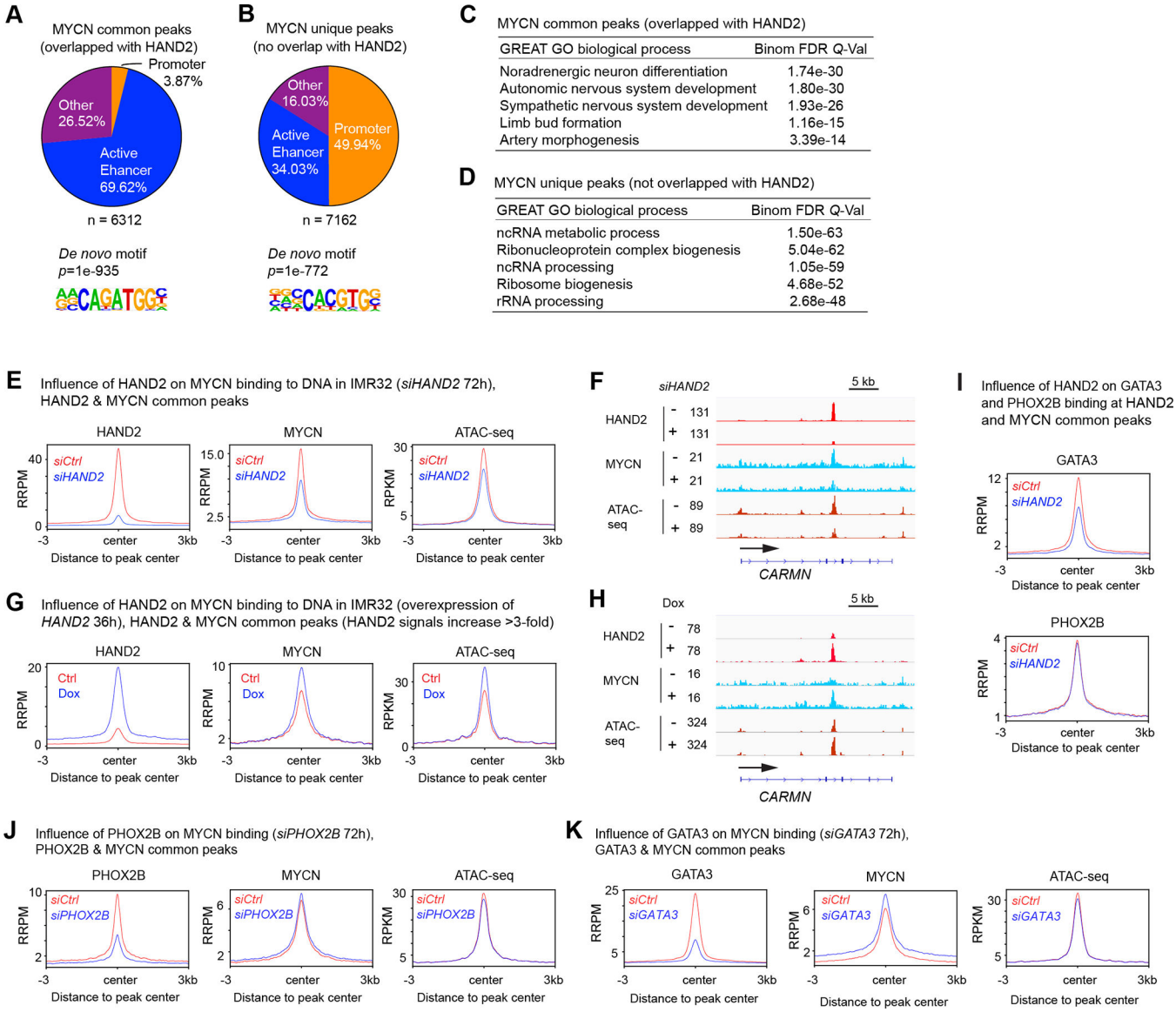

Figure 2. HAND2 assists MYCN to bind to DNA.

(A) Venn diagram shows the distribution of MYCN binding sites that overlapped with HAND2 binding sites in IMR32 cells (top panel). Motif scan shows that the MYCN binding motif is a non-canonical E-box. (B) Venn diagram shows the distribution of MYCN unique binding sites in IMR32 cells. Motif scan shows that the MYCN binding motif is a canonical E-box. (C) GO analysis of MYCN and HAND2 overlapped peaks associated genes. (D) GO analysis of MYCN unique peaks associated genes. (E) Composite profile of ChIP-seq data shows the average ChIP-seq signal of MYCN and ATAC-seq signal after the knockdown of *HAND2* for 72 h in IMR32 cells. (F) Signal tracks show that the knockdown of *HAND2* results in a decrease of MYCN signal and ATAC-seq signal within the *CARMN* gene locus. (G) Composite plots show that the overexpression of *HAND2* in IMR32 cells for 36 h results in an increased average ChIP-seq signal of MYCN that accompanied by an increase of average ATAC-seq signal. (H) Signal tracks show that the overexpression of *HAND2*

results in an increased MYCN signal and ATAC-seq signal within the *CARMN* gene locus. (I) Composite plots show a decreased average GATA3 ChIP-seq signal but no change of PHOX2B signal after knocking down *HAND2* in IMR32 cells for 72 h. (J-K) Composite plots show the influence of the knockdown of *PHOX2B* ofr *GATA3* in IMR32 cells for 72 h on the average ChIP-seq signal of MYCN and ATAC-seq signal. RRPM: spike-in normalized, reference-adjusted reads per million mapped reads; RPKM: reads per kilobase per million mapped reads.

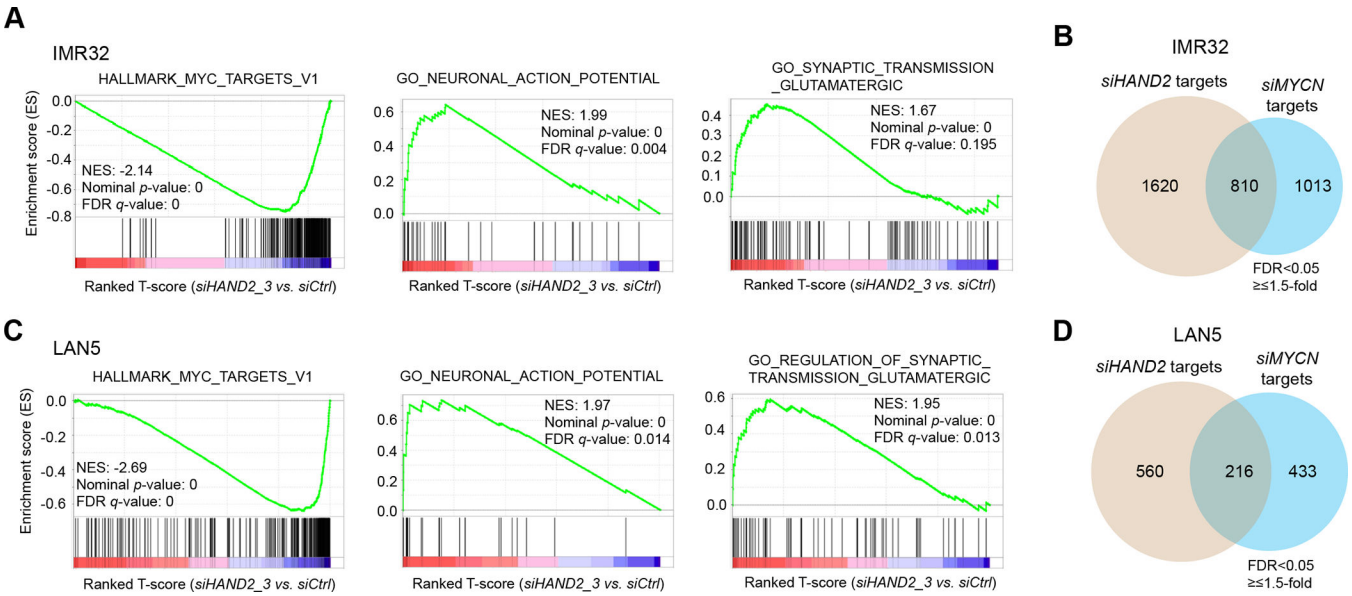

Figure 3. HAND2 regulates the expression of a large subset of *MYCN* targets.

(A) GSEA shows a negative enrichment of MYC signature genes, and a positive enrichment of neuronal genes after the silencing of *HAND2* in IMR32 cells for 72 h. (B) Venn diagram shows that around 45% genes regulated by MYCN is also regulated by HAND2 in IMR32 cells. (C) GSEA shows a negative enrichment of MYC signature genes, and a positive enrichment of neuronal genes after knockdown of *HAND2* in LAN5 cells for 72 h. (D) Venn diagram shows that around 33% genes regulated by MYCN is also regulated by HAND2 in LAN5 cells.

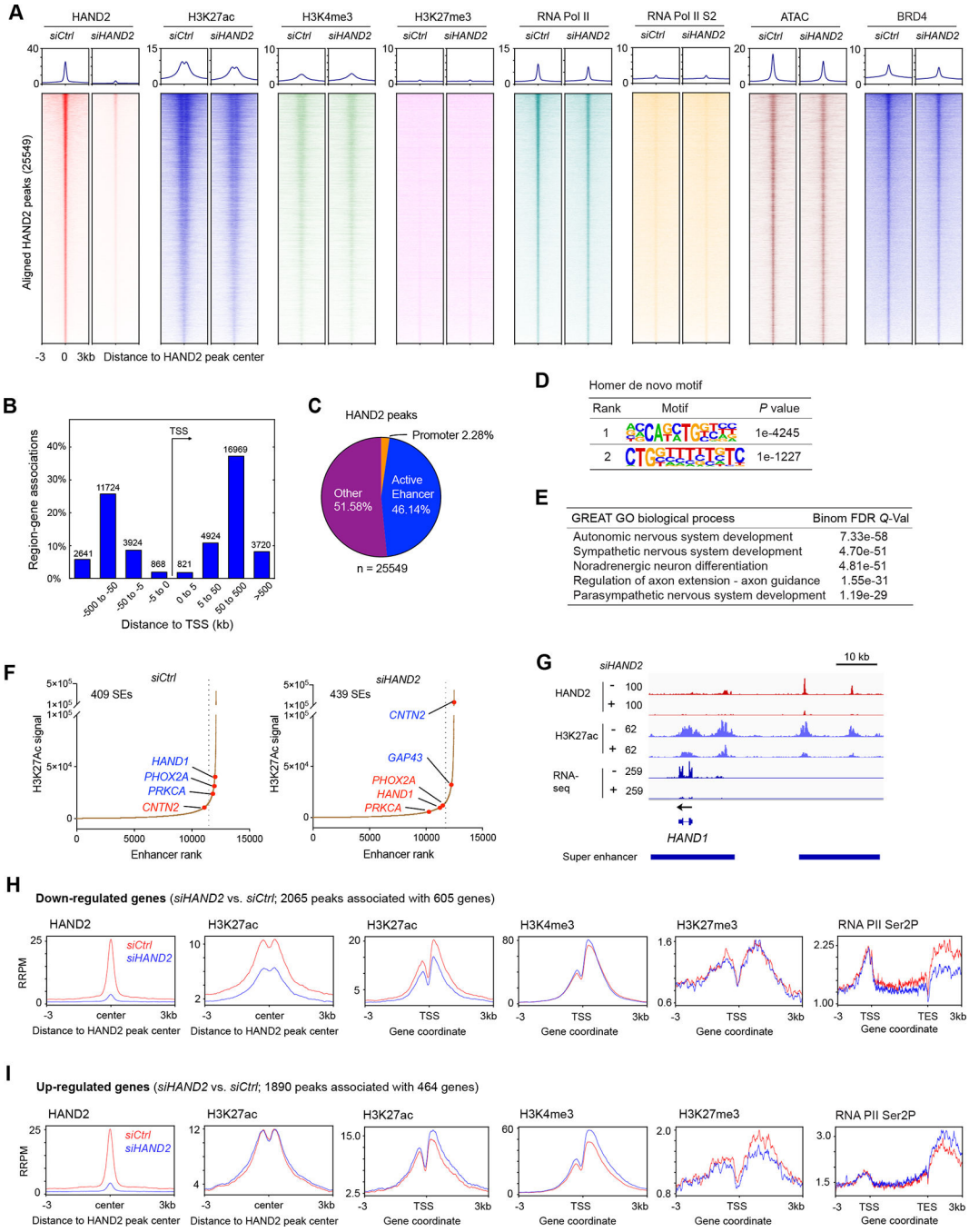

Figure 4. Loss of *HAND2* affects regional epigenetic modification.

(A) Heatmaps of ChIP-seq data at the ranked HAND2 peak center before (*siCtrl*) and after (*siHAND2*) knocking down of *HAND2* for 72 h in IMR32 cells. (B) HAND2 peak distribution determined by prediction tool GREAT. (C) Venn diagram shows that around 46% of HAND2 binding sites are at active enhancer regions (overlapping with H3K27ac binding sites). (D) Motif scan shows the enrichment of two known HAND2 binding motifs. (E) HAND2 binding sites associated genes identified by GREAT GO analysis. (F) The silencing of *HAND2* affects super-enhancers establishment. (G) Signal tracks show that

the knockdown of *HAND2* decreased signal of H3K27ac and RNA-seq at the *HAND1* gene locus. (H-I) Composite plots show the changes of the average ChIP-seq signals of the indicated proteins after the knockdown of HAND2 for 72 h in IMR32 cells.

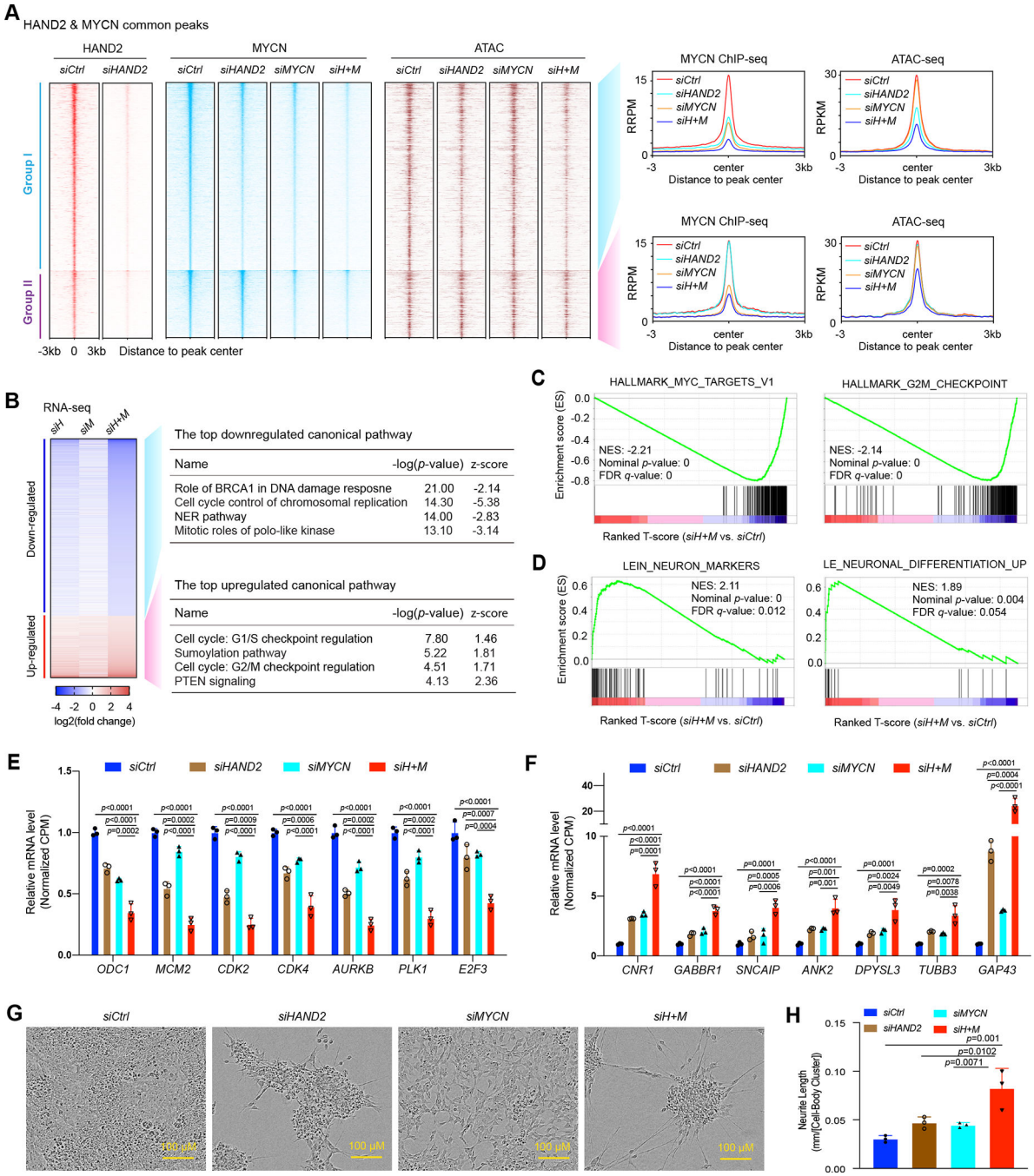

Figure 5. HAND2 and MYCN cooperatively regulate chromatin accessibility and gene transcription.

(A) Heatmaps (left panel) and composite profiles (right panel) of ChIP-seq and ATAC-seq results before and after the knockdown of *HAND2* (*siHAND2*), *MYCN* (*siMYCN*) or both (*siH+M*) in IMR32 cells (72 h). (B) Heatmap shows that the knockdown of both *HAND2* and *MYCN* using siRNAs (*siH+M*) results in greater effect on the down- or up- regulation of gene expression than knocking down each one alone (*siH* or *siM*) in IMR32 cells (72 h). Ingenuity canonical pathway analysis shows the associated pathways of these downregulated and upregulated genes. (C) GSEA shows that the knockdown of

both *HAND2* and *MYCN* results in a negative enrichment of *MYC* target genes and genes involved in G2M checkpoint. (D) GSEA shows that the knockdown of both HAND2 and MYCN results in a positive enrichment of neuron markers and neuronal differentiation genes. (E-F) The silencing of both of *HAND2* and *MYCN* results in a more significant downregulation of genes that required for G2M progression and upregulation of neuronal differentiation genes based on the RNA-seq results. CPM: counts per million. (G-H) The knockdown of both *HAND2* and *MYCN* results in a significant increase of neurite length shown by the cell image and the IncuCyte neurite-length assay.

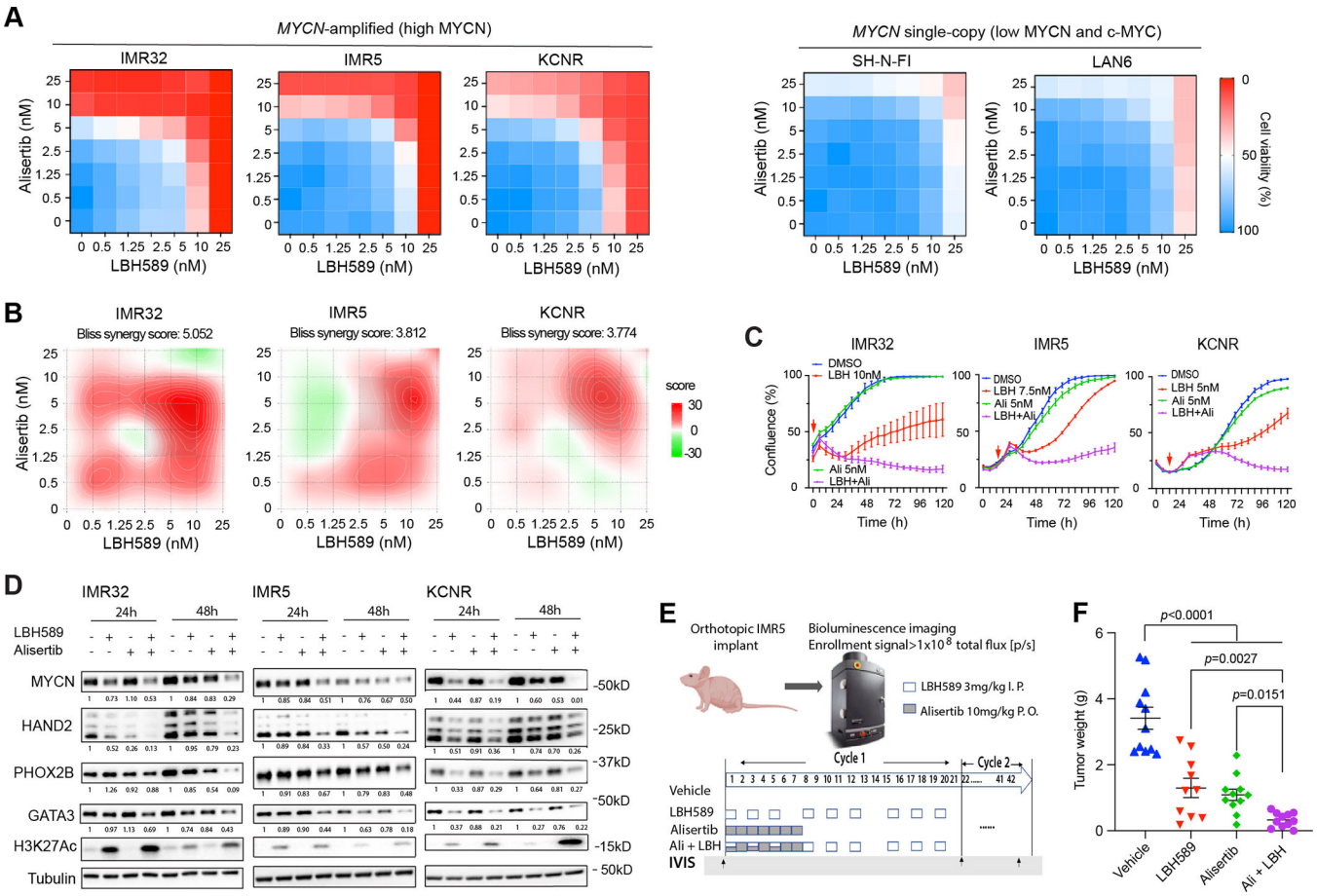

Figure 6. Targeting both MYCN and CRC TFs.

(A) Heatmaps show the percentage of cell viability after different dose of HDAC inhibitor LBH589 and Aurora A kinase inhibitor alisertib treatment in NB cell lines. Cell viability is measured by CellTiter-Glo Cell Viability Assay after 72 h drug treatment. (B) SynergyFinder online tool is used for bliss synergistic analysis to evaluate the synergistic effect of the combination treatment in *MYCN*-amplified cell lines shown in (A). (C) IncuCyte cell confluence assays show the synergistic effect of the alisertib (Ali) + LBH589 (LBH) treatment on cell proliferation (% confluency) over time. The red arrow is the time point of adding compounds. (D) Western blot analysis shows the protein levels of MYCN and CRC TFs in NB cells treated with LBH589 (LBH, 7.5 nM for IMR32, 7.5 nM for IMR5 and 5 nM for KCNR), alisertib (Ali, 2 nM for IMR32, 5 nM for IMR5 and 5 nM for KCNR) alone or in combination for 24 h and 48 h. (E) Schematic diagram to show the strategy of drug treatment in orthotopic IMR5-GFP-Luc implanted xenografts. IVIS: *in vivo* imaging system. (F) Tumor weight measurement shows a significant decrease of the tumor weight of the drug treatment groups compared to the tumor weight of the vehicle treatment group. The *p*-value indicated is calculated in one-way ANOVA.

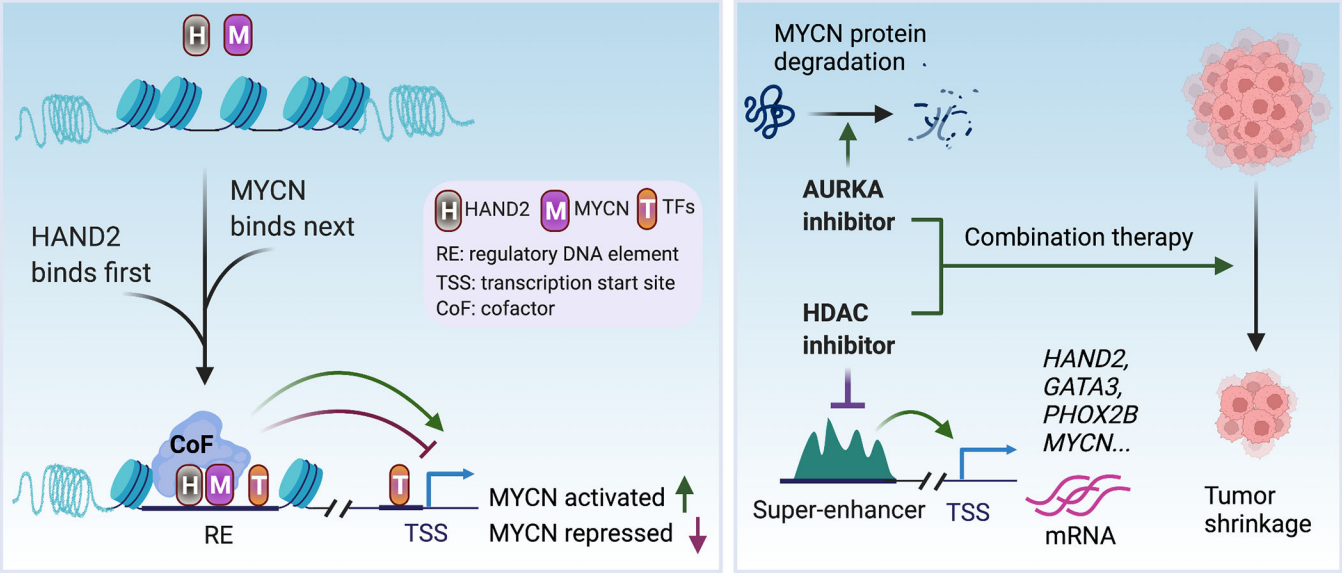

Figure 7.
The cooperation between HAND2 and MYCN makes them ideal therapeutic targets.